Understanding the atmospheric response to seismic sources: the 2020 m_b 4.9 Kiruna minequake, Sweden

Antoine Turquet [https://orcid.org/0000-0003-1920-935X][1], Quentin Brissaud [https://orcid.org/0000-0001-8189-4699][1], Sven Peter Näsholm [https://orcid.org/0000-0001-9107-4002][1,2], Johan Kero [https://orcid.org/0000-0002-2177-6751][3], and Alexis Le Pichon [https://orcid.org/0000-0001-6531-069X][4]

[1]NORSAR, Gunnar Randers vei 15, Kjeller, Norway
[2]Department of Informatics, University of Oslo, P.O. Box 1080, NO–0316 Oslo, Norway
[3]Swedish Institute of Space Physics (IRF), Kiruna, Sweden
[4]CEA, DAM, DIF, F-91297 Arpajon, France

1 Atmospheric model construction

Similar to Brissaud et al. (2023), atmospheric models are built as the combination of ERA-5 reanalysis models up to 80 km altitude together with MSIS and HWM14 models for upper background atmospheric conditions and winds up to 120 km altitude. In order to account for unresolved wind perturbations in the stratosphere, we construct gravity-wave perturbations using Gardner's model. Gardner's model characterizes the horizontal wave number spectra of wind perturbations assuming that both saturated and unsaturated waves obey the polarization and dispersion relations, and that the vertical wave number and temporal frequency are separable. The implemented horizontal wave number spectrum allows calculating the horizontal correlation lengths of the wind perturbations. Random realizations of range dependent perturbation terms are obtained and superimposed to the effective sound speed profiles in the propagation plane.

2 TL inversion methodology

Transmission Loss (TL) distributed over the region close to epicenter provides good insight of how the seismo-acoustic coupling may have happened during the event. We can obtain TLs in the near-field, assuming a direct linear propagation, by backprojecting infrasound amplitudes over a grid around the epicenter. For inversion, we have used the following characteristic information of the minequake: origin

time at 01:11:56.2 UTC with an error ±3 m/s, sound velocity $c_s = 330 \pm 8$ m/s, and backazimuth error $e_{\text{baz}} = \pm 5$ degrees. The epicenter is located at (67.83965°N, 20.20759°E) and the station KRIS is located at (67.8549°N, 20.4220°E). To incorporate the possible error in backazimuth and origin time, we have perturbed our input parameters with a uniform distribution with 10 realizations. For the errors in backpropagation velocity, we have used normal distribution with 330 ± 8 m/s having a standard deviation 0.008 m/s and 15 realizations. The amplitudes and backazimuths are obtained from PMCC analysis (i.e., pixels in PMCC) of station KRIS between 01:12:15 - 01:12:50 UTC. To correct for the propagation in solid earth, we have used $\Delta d = \sqrt{\frac{-h}{1-(\frac{v_s}{v_a})^2}}$ where Δd is the distance correction for the propagation time in solid earth, h is the focal depth, v_s is the seismic velocity, v_a is the acoustic velocity. The corrected propagating distances were used to correct amplitudes for spherical spreading and converted to Transmission Loss (TL) using the formula $TL = 20log_{10}(A/A_r)$ where A is the distance corrected amplitude, A_r is the reference amplitude (1 Pa) (Walker et al., 2011). Computed TL over multiple distances and probabilities were grouped over the predefined mesh and sorted according to their probabilities in each grid. TL having the maximum probability is chosen and plotted over the map.

3 Geometrical spreading correction

Waveforms are simulated in 2d using SPECFEM-DG and therefore require a phase and amplitude correction due to 3d geometrical spreading effects. We adopt a simple procedure described in Miksat et al. (2008) that consists of convolving 2d waveforms with a time- and velocity-dependent correction. This formulation relies on the assumptions that the media are homogeneous, and that the sources, for both acoustic and seismic waves, are point sources in space.

In a homogeneous acoustic medium, the ratio of 3d-to-2d Green's functions (equivalent to a 3d-to-2d ratio of fundamental-mode Rayleigh waves) gives us the correction factor C in the frequency domain (see eq. (13) in Miksat et al. (2008)),

$$C(w) = \sqrt{\frac{|w|}{2\pi cr}} e^{-\frac{i\pi sign(w)}{4}}, \tag{1}$$

where $w = 2\pi f$, where f (Hz) is the frequency, c (m/s) is the medium velocity, and r (m) is the source-receiver distance. We can then compute the 3d corrected waveform as,

$$s_{3d}(t,r) = \mathbb{F}^{-1}(C(w)\mathbb{F}(s_{2d}(t,r))), \tag{2}$$

where s_{2d} (Pa) is the waveform from 2d simulations, $\mathbb{F}$ is the Fourier transform, and s_{3d} (Pa) is the 3d-corrected waveform.

Because this procedure depends on the medium velocity, we perform the scaling of seismic waves and acoustic waves independently by assuming a seismic wave velocity of $c_s = 3.5$ km/s, and an acoustic wave velocity of $c_a = 0.34$ km/s. The seismic velocity is taken as an upper bound of the Rayleigh wave velocity in the frequency range of interest as Rayleigh waves dominate the recordings at KRIS. Although surface wave velocity is frequency dependent, the impact of small variations in seismic velocities (± 0.5 km/s) in the scaling procedure, described in eq. 1 and 2, impact the phase amplitude by less than 10%.

4 Impact of topography, source location, and subsurface properties on near-field infrasound signals

Various frequency-dependent contributions along the seismo-acoustic propagation path can affect the infrasound waveforms (Brissaud et al., 2021): Topography through wave scattering, subsurface seismic velocities that affects the coupling efficiency, and focal depth and epicenter. In order to assess their influence in the case of the Kiruna minequake, we considered various scenarios: (1) low- and high- frequency simulations without topography to investigate the impact of topography vs frequency, (2) a low-frequency simulation with a source South of the mine which differs from the dominating collapse event epicenter, and (3) a high-frequency simulation with a sedimentary layer to showcase the impact of unconsolidated material on wave transmission. Simulation parameters are shown in Table 1 and seismic velocity models are described in Supp Section 5.

Owing to the smoothness of the local topography, it has an insignificant impact on both amplitude and phase of low-frequency signals (Fig. 1) but impacts the later seismic and acoustic arrivals at higher frequencies (Fig. 2). Epicenter location mostly delays the arrival of both seismic and acoustic waves by increasing the travel time (Fig. 1) since the collapse source is dominated by its isotropic component. At high frequencies, focal depth significantly impact the amplitude of both seismic and acoustic arrivals with shallower sources transmitting more energy to the atmosphere (Fig. 2). A sedimentary layer drastically increase the amplitude of both seismic and acoustic waves by exciting trapped waves in the shallow sedimentary layer.

5 Seismic velocity model

The 1D seismic velocity model used for moment-tensor inversion and seismo-acoustic full-waveform simulations is described in Table 2. The 1D model with a sedimentary layer used in Section 4 is described in Table 3.

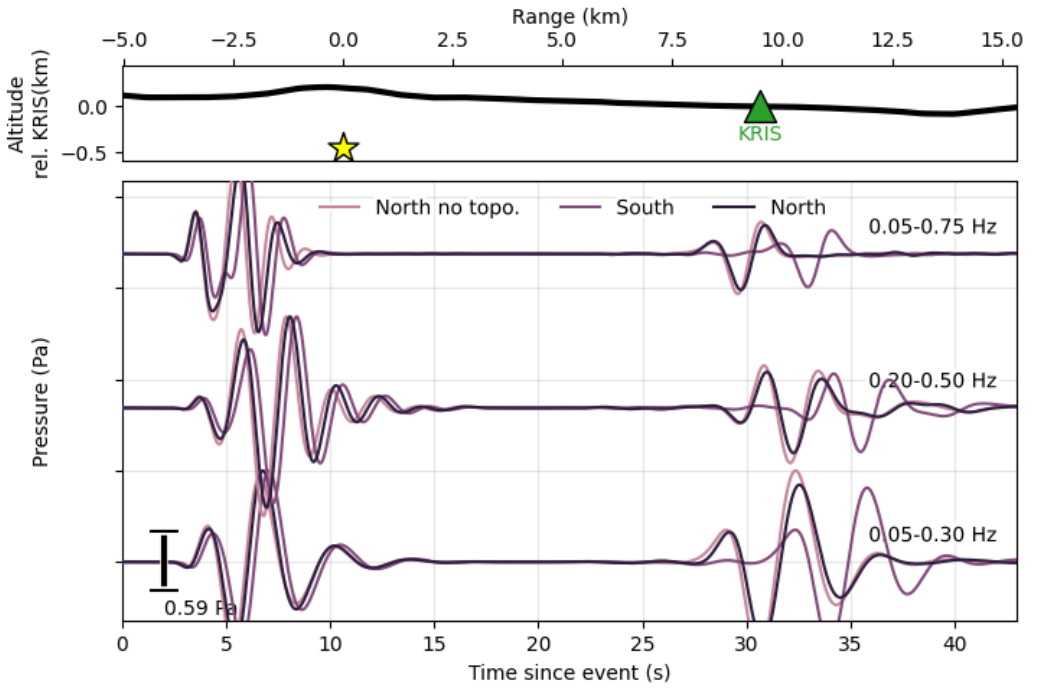

Figure 1. Simulated acoustic waveforms at KRIS for a low-frequency source at focal depth 0.5 km located North of the mine with topography (black) and without (light pink), and for a source located South of the mine (purple). Simulations parameters can be found in Table 1.

Source location	Corner frequency (Hz)	Focal depth (km)	Topography	Sediments	Reference
North	0.75	0.5	No	No	light pink Fig. 2
North	0.75	0.5	Yes	No	black Fig. 1
South	0.75	0.5	Yes	No	purple Fig. 1
South	1.75	0.5	Yes	No	dark blue Fig. 1
North	1.75	0.5	No	No	dark green Fig. 2
North	1.75	0.5	Yes	Yes	green Fig. 2
North	1.75	0.1	Yes	No	red Fig. 2

Table 1. Simulation parameters used for the sensitivity analysis in Supplementary Sec. 4. North source location refers to latitude and longitude (67.8397°N, 20.2076°E). South source location refers to latitude and longitude (67.8251°N, 20.1891°E). The source time function is a Gaussian function. The moment tensor model corresponds the solution presented in the moment tensor analysis in the main text.

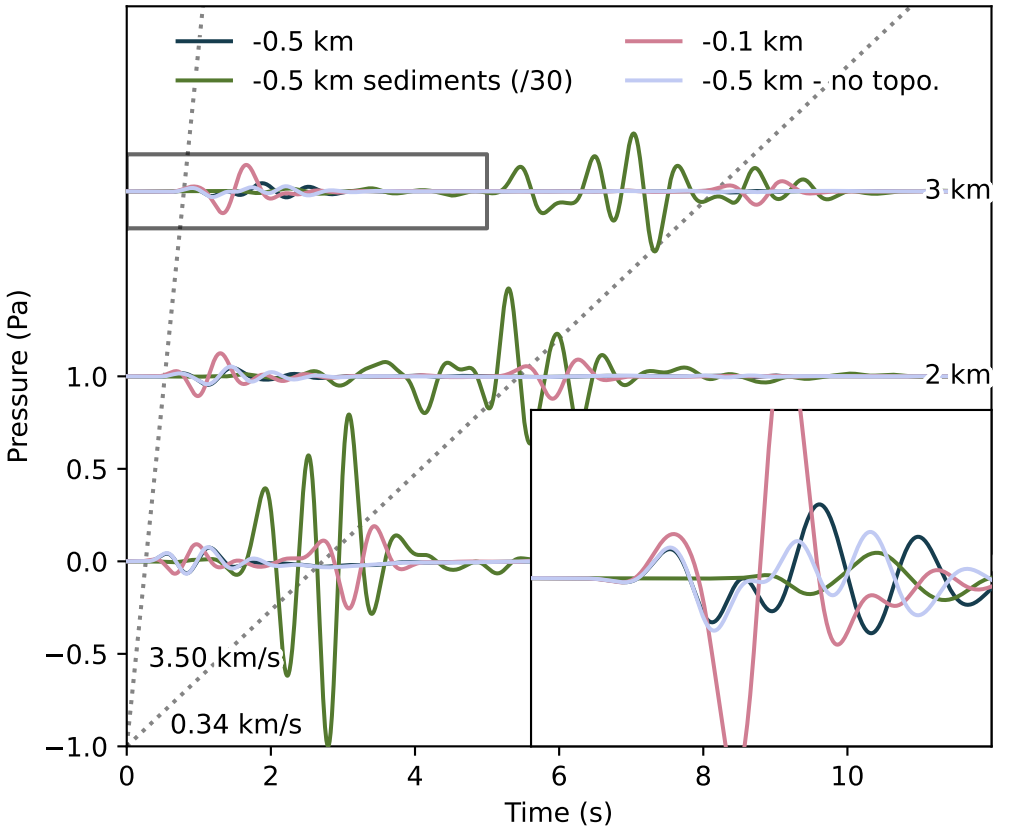

Figure 2. Simulated acoustic waveforms at KRIS for a high-frequency source at focal depth 0.5 km (dark blue, green, light purple) or 0.1 km (light red), without topography (light purple), and with a sedimentary layer (amplitude divided by 40, green). Simulation parameters can be found in Table 1.

Thickness (km)	V_s (km/s)	V_p (km/s)	ρ (kg/m^3)	Q_s	Q_s
0.01	0.55	2.00	1.93	500	1000
1.96	2.70	5.00	2.55	500	1000
3.94	3.70	6.50	2.85	500	1000
13.76	4.05	7.10	3.05	500	1000
1000	4.28	7.68	3.17	500	1000

Table 2. 1D seismic velocity derived from CRUST1.0. V_s (km/s) is the shear velocity. V_p (km/s) is the compressional velocity. ρ is the density. Q_s and Q_p are the shear- and compressional-wave quality factors.

Thickness (km)	V_s (km/s)	V_p (km/s)	ρ (kg/m^3)	Q_s	Q_s
0.25	0.55	2.00	1.93	500	1000
1.96	2.70	5.00	2.55	500	1000
3.94	3.70	6.50	2.85	500	1000
13.76	4.05	7.10	3.05	500	1000
1000	4.28	7.68	3.17	500	1000

Table 3. 1D seismic velocity derived from CRUST1.0 with sedimentary layer. V_s (km/s) is the shear velocity. V_p (km/s) is the compressional velocity. ρ is the density. Q_s and Q_p are the shear- and compressional-wave quality factors.

6 Details about the moment-tensor inversion

In this Section, we provide more details about the best moment tensor solution described in Sec. 2 in the main text. Figure 3 shows all waveform fits for our best moment-tensor solution. A summary of the distribution of moment tensor solutions and corresponding accuracies to reproduce observed waveforms is show in Fig. 4.

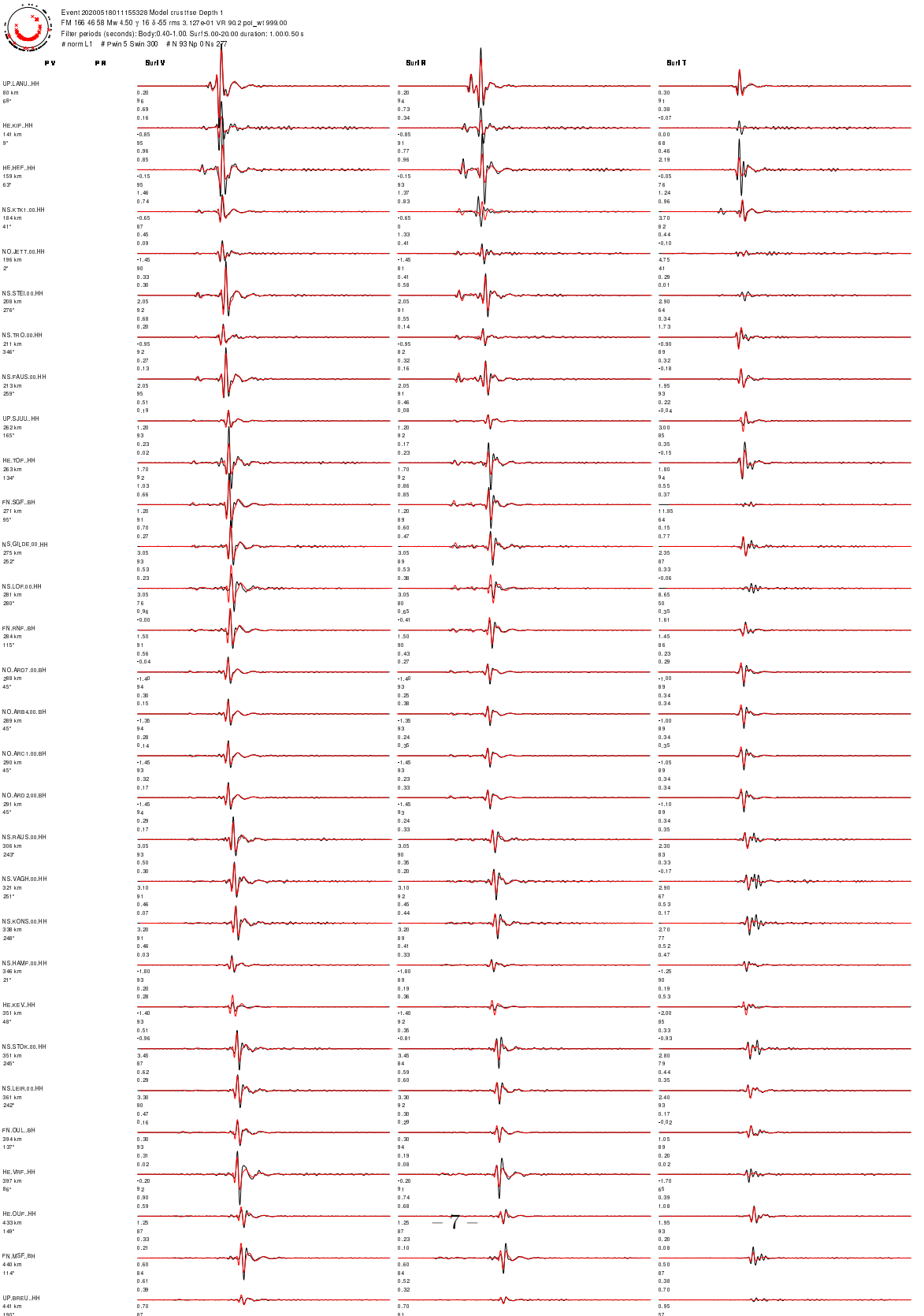
Event 20200518011155328 Model crust1se Depth 1
FM 166 46 58 Mw 4.50 γ 16 δ -55 rms 3.127e-01 VR 90.2 pol_wt 999.00
Filter periods (seconds): Body:0.40-1.00 Surf:5.00-20.00 duration: 1.00/0.50 s
norm L1 # Pwin 5 Swin 300 # N 93 Np 0 Ns 277
P V
P R
Surf V
Surf R
Surf T
UP.LANU..HH
80 km
68°
HE.KIF..HH
141 km
9°
HE.HEF..HH
159 km
63°
NS.KTK1.00.HH
184 km
41°
NO.JET1.00.HH
196 km
2°
NS.STEI.00.HH
208 km
276°
NS.TRO.00.HH
211 km
346°
NS.FAUS.00.HH
213 km
259°
UP.SJUU..HH
262 km
165°
HE.TOF..HH
263 km
134°
FN.SGF..BH
271 km
95°
NS.GILDE.00.HH
275 km
252°
NS.LOF.00.HH
281 km
280°
FN.RNF..BH
284 km
115°
NO.ARD7.00.BH
288 km
45°
NO.ARB4.00.BH
289 km
45°
NO.ARC1.00.BH
290 km
45°
NO.ARD2.00.BH
291 km
45°
NS.RAUS.00.HH
306 km
243°
NS.VAGH.00.HH
321 km
251°
NS.KONS.00.HH
338 km
248°
NS.HAMF.00.HH
346 km
21°
HE.KEV..HH
351 km
48°
NS.STOK.00.HH
351 km
245°
NS.LEIR.00.HH
361 km
242°
FN.OUL..BH
394 km
137°
HE.VRF..HH
397 km
96°
HE.OUF..HH
433 km
148°
FN.MSF..BH
440 km
11°
UP.BREU..HH
441 km
190°

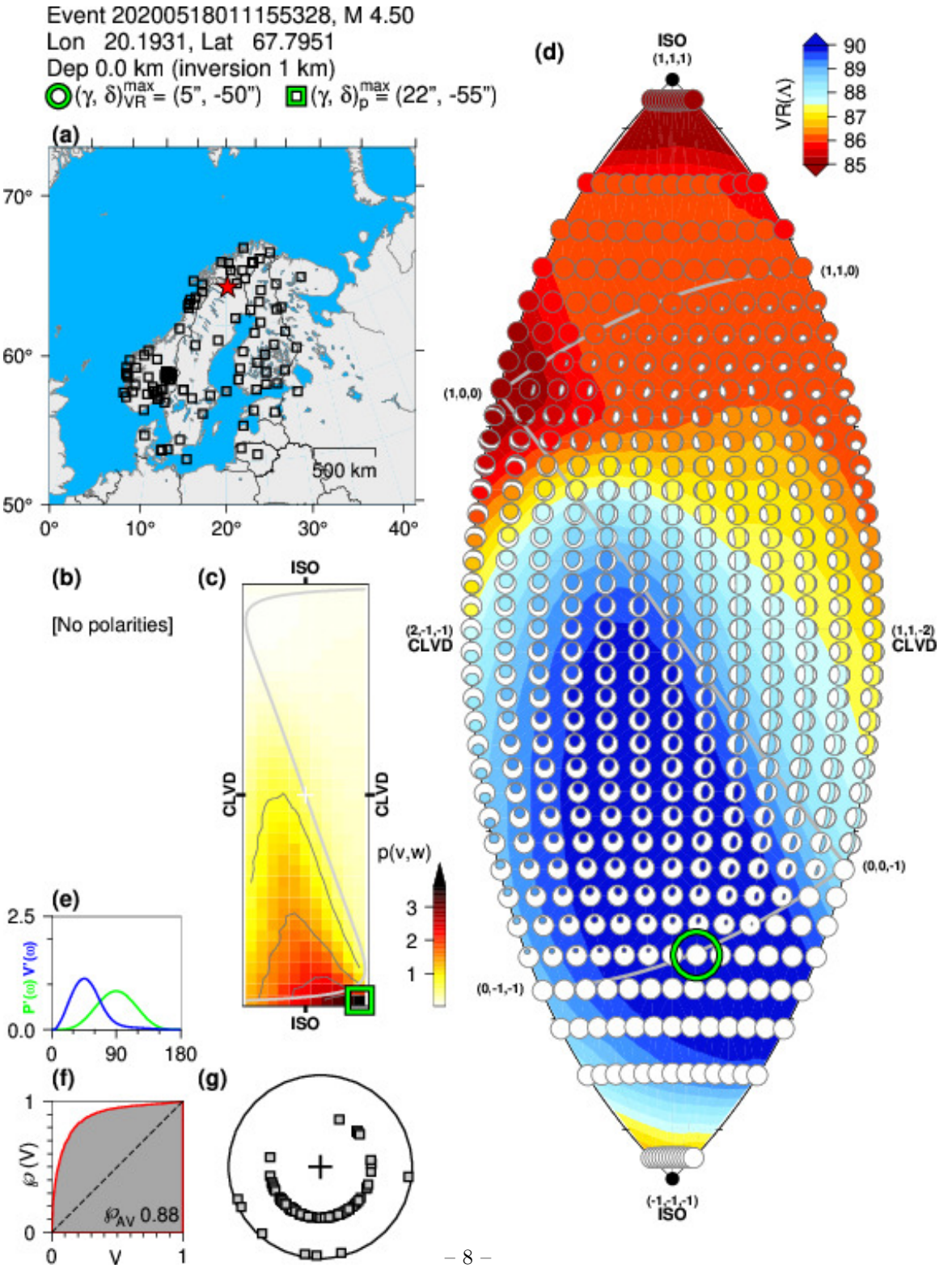
Event 20200518011155328, M 4.50
Lon 20.1931, Lat 67.7951
Dep 0.0 km (inversion 1 km)
(γ, δ)VR max = (5", -50")
(γ, δ)p max = (22", -55")
(a)
70°
60°
50°
0°
10°
20°
30°
40°
500 km
(b)
[No polarities]
(c)
ISO
CLVD
CLVD
ISO
p(v,w)
3
2
1
(d)
ISO
(1,1,1)
VR(Λ)
90
89
88
87
86
85
(1,1,0)
(1,0,0)
(2,-1,-1)
CLVD
(1,1,-2)
CLVD
(0,0,-1)
(0,-1,-1)
(-1,-1,-1)
ISO
(e)
2.5
0.0
P'(ω) V'(ω)
0
90
180
(f)
1
0
℘ (V)
℘AV 0.88
0
V
1
(g)

Figure 4. XXX

References

Q. Brissaud, S. Krishnamoorthy, J. M. Jackson, D. C. Bowman, A. Komjathy, J. A. Cutts, Z. Zhan, M. T. Pauken, J. S. Izraelevitz, and G. J. Walsh. The first detection of an earthquake from a balloon using its acoustic signature. *Geophysical Research Letters*, 48(12):e2021GL093013, 2021. https://doi.org/10.1029/2021GL093013.

Q. Brissaud, S. P. Näsholm, A. Turquet, and A. Le Pichon. Predicting infrasound transmission loss using deep learning. *Geophysical Journal International*, 232(1):274–286, 2023.

J. Miksat, T. Müller, and F. Wenzel. Simulating three-dimensional seismograms in 2.5-dimensional structures by combining two-dimensional finite difference modelling and ray tracing. *Geophysical Journal International*, 174(1):309–315, 2008.

K. T. Walker, R. Shelby, M. A. H. Hedlin, C. d. Groot-Hedlin, and F. Vernon. Western U.S. infrasonic catalog: illuminating infrasonic hot spots with the USArray. *Journal of Geophysical Research: Solid Earth*, 116(B12), 2011. ISSN 2156-2202. https://doi.org/10.1029/2011JB008579.